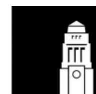

UNIVERSITY OF LEEDS

This is a repository copy of *Exploring the formation of intrinsic p-type and n-type defects in CuO*.

White Rose Research Online URL for this paper:
https://eprints.whiterose.ac.uk/165237/

Version: Accepted Version

Article:

Živković, A and de Leeuw, NH orcid.org/0000-0002-8271-0545 (2020) Exploring the formation of intrinsic p-type and n-type defects in CuO. Physical Review Materials, 4 (7). 074606. ISSN 2475-9953

https://doi.org/10.1103/physrevmaterials.4.074606

©2020 American Physical Society. This is an author produced version of an article published in Physical Review Materials. Uploaded in accordance with the publisher's self-archiving policy.

Reuse
Items deposited in White Rose Research Online are protected by copyright, with all rights reserved unless indicated otherwise. They may be downloaded and/or printed for private study, or other acts as permitted by national copyright laws. The publisher or other rights holders may allow further reproduction and re-use of the full text version. This is indicated by the licence information on the White Rose Research Online record for the item.

Takedown
If you consider content in White Rose Research Online to be in breach of UK law, please notify us by emailing eprints@whiterose.ac.uk including the URL of the record and the reason for the withdrawal request.

eprints@whiterose.ac.uk
https://eprints.whiterose.ac.uk/

Exploring the formation of intrinsic *p*-type and *n*-type defects of CuO

Aleksandar Živković[1,2] and Nora H. de Leeuw[2,3,*]

[1] *Cardiff University, School of Chemistry, Main Building Park Place, Cardiff CF10 3AT, United Kingdom*
[2] *Department of Earth Sciences, Utrecht University, Princetonlaan 8a, 3548CB Utrecht, The Netherlands*
[3] *School of Chemistry, University of Leeds, Woodhouse Lane, Leeds LS2 9JT, United Kingdom*
[*] *Corresponding author: N.H.deLeeuw@leeds.ac.uk*

Abstract

CuO (cupric oxide) is a well known *p*-type semiconductor, suitable for solar cell photovoltaic applications. However, due to the easy formation of defects and Cu-rich layers at the copper(II) oxide hetero-interface, commercial application is yet to be successfully implemented. Density functional theory calculations have been employed to study the formation of intrinsic defects and their effect on the electronic properties of CuO. Native impurities were observed, depending on the synthesis conditions, to render the conductivity to *p*-type or *n*-type at a low energetic cost, yet with states embedded deep in the electronic band gap. Respective defect pairs, effectively determining the majority charge carriers, were observed to cluster in near proximity of each other, lowering the formation energy substantially. Hydrogen passivation was illustrated to have a positive effect on deep defect states in *p*-type CuO, without affecting the *n*-type counterpart. Outlined results were found to support the experimentally observed low photo-response of CuO and further illustrate some of the difficulties related with achieving high-performance samples.

1 Introduction

Copper(II) oxide (CuO) is a strongly correlated transition metal oxide which shows active coupling between spin, charge, orbital, and vibrational degrees of freedom. It has been studied intensively since the discovery of cuprate high-temperature superconductors, due to the close resemblance of its structural, electronic, and magnetic properties [1–4]. In CuO, low-energy physics induces antiferromagnetism with two distinct Néel temperatures and multiferroicity, reflecting the presence of competing equilibrium phases lying close to each other in energy [5–7].

CuO is a *p*-type semiconductor, with promising potential as a non-toxic, stable, and abundant material for photovoltaic (PV) and photocatalytic applications. Owing to its favourable electronic band gap value of 1.4 eV [8–10], it was postulated as an ideal candidate for solar harvesting technologies. However, reports on CuO solar cells are relatively rare and the obtained power conversion efficiencies (PCE), of incident sunlight into usable electric currents,

yield values which are an order of magnitude lower than the estimated potential value based on the Shockley-Queisser limit (around 30 %) [11]. As demonstrated earlier [12–14], one single ideal value does not guarantee good applicability for solar harvesting (especially for oxides of copper), as this neglects a multitude of other factors (recombination, strong absorption onset, charge carrier lifetimes, etc.).

In practice, many photovoltaic energy converters use semiconducting materials in the form of a *p*-*n* or *p*-*i*-*n* junction. Structures of heterojunction solar cells with *p*-type CuO typically involve *n*-type Si, although their efficiencies measure values below 0.5 % [15]. The low performance was attributed to the formation of Cu-rich copper oxide, as well as an amorphous interfacial oxide layer occurring between CuO and Si. Slight improvement was observed in Al/Ti/*n*-Si/*p*-CuO/Ti/Al heterostructure solar cells, approaching efficiencies of 1 % [16]. Doping CuO with N and interfacing with *n*-Si was observed to improve the efficiency to 1.21 %, as a result of improved crystallinity and thinning of the interfacial Cu-rich layer [17].

It was not until recent that *n*-type CuO has been observed. This conductivity type, driven by an excess number of electrons, was detected in nanoscale non-stoichiometric CuO_x deposited by reactive magnetron sputtering [18]. By depositing *n*-CuO_x onto hydrogenated amorphous Si, efficiencies of 3.04 % and 4.78 % were observed. Efficiency values were enhanced because in this case the interfacial Cu-rich layer acts as an electron supply reservoir instead of a recombination source for holes in *p*-CuO.

Du *et al* [19] have reported single phase intrinsic *n*-type CuO films prepared by magnetron sputtering combined with a high-voltage and low-current technique. Increasing the substrate temperature was found to convert CuO from a *p*-type semiconductor at 75° C (348 K) to an *n*-type semiconductor at 500° C (773 K). The *n*-type conductivity was assigned to oxygen vacancies and interstitial copper atoms. Enhanced point-defect scattering rates with increasing temperature were identified as the main cause of the decrease in overall carrier mobility rates with increasing temperature. Singh *et al* [20] have reported the successful deposition of *n*-type CuO via spin-coating. *n*-type CuO was created at moderate oxygen partial pressures (metal excess phase), leaving the material oxygen–deficient in the form of oxygen vacancies. The annealing time was reported to be a crucial parameter, with CuO changing into Cu_2O over a prolonged time. Further studies of *n*-type CuO included extrinsic impurity–driven conductivity change. Baturay and co-workers [21] observed *p*-type conductivity conversion into *n*-type in CuO thin films when doped with Co. Capacity–voltage measurements verified a change in polarity at 3 % doping ratio, with no change in the band gap. Moreover, Wang *et al* [22] observed increased charge separation and transfer in a CuO semiconducting photocathode as a results of a simple O_2 treatment which rendered the material's conductivity *p*-type.

Theoretically, despite a substantial number of publications studying the ground state properties of CuO, the intrinsic defects still remain largely unexplored. Nolan *et al* [23] and Wu *et al* [24] studied the native defects within CuO using LSDA+U calculations. However, defects were studied in the conventional monoclinic cell and simple antiferromagnetic configuration, not necessarily corresponding to the experimentally observed ground state. More recent, Wang *et al* [22] explored the influence of copper vacancies in CuO based photocathodes using GGA(PBE)+U calculations. Nonetheless, none of the reported studies concerning the formation of defects in

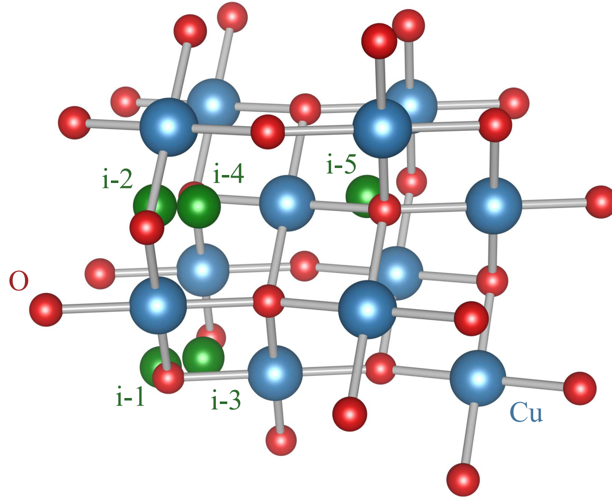

Figure 1: Crystal structure of the magnetic unit cell of CuO together with the five identified suitable positions for interstitial atoms.

CuO did not take into account the formation of competing phases, namely Cu_2O and Cu_4O_3, thereby most likely representing growth conditions for unphysical CuO compositions.

In the current work, native point defects, both simple and complex, were initialized within the magnetic unit cell of CuO and their formation energies, as well as influence on the overall electronic band structure explored. In order to do so, a comparative density functional theory study was undertaken using Hubbard–corrected and hybrid exchange correlation functional approximations. An attempt to answer some of the following questions is made: (i) which defects occur intrinsically in CuO and which computational method describes them accurately? (ii) does the model address the origin of experimentally observed n-type conductivity and, if so, under which conditions?

2 Computational details

The results computed and presented in this work were were obtained from spin-polarized DFT-based calculations performed with the Vienna Ab-initio Simulation Package (`VASP`) [25]. The interactions between core and valence electrons were represented using the projector augmented wave (PAW) method [26]. The general gradient approximation (GGA) [27] exchange-correlation (XC) functional with the Perdew–Burke–Ernzerhof (PBE) parametrization was employed for DFT+U within the formalism of Dudarev *et al* [28]. For the hybrid-DFT calculations, the HSE XC functional was used [29–31], with a screening parameter of $0.2\,\text{Å}^{-1}$. Long distance dispersion corrections were included using the D3 approach of Grimme *et al* [32]. The plane wave expansion cutoff was set to 450 eV and the force convergence criterion to cell relaxation was 0.01 eV/Å. Γ-centred Monkhorst-Pack [33] meshes ($3 \times 5 \times 3$ for magnetic unit cell and a single Γ-point for the $2 \times 3 \times 2$ supercell) were employed to sample the Brillouin zone in reciprocal space. Band structure calculations were performed on the optimized structure along high-symmetry directions obtained from the Bilbao Crystallographic Server [34–36] and plotted

103 using the `Wannier90` code [37, 38]. The phase stability diagram of CuO for a range of ac-
104 cessible chemical potentials was computed using CPLAP (Chemical Potential Limits Analysis
105 Program)[39], taking into account its limiting competing phases. The extent of defect charge
106 distribution was studied using the Bader scheme as implemented in the Henkelman code [40–42].
107 Suitable defect positions were identified using the `PyCDT` package [43] Graphical drawings were
108 produced using VESTA [44].

109 The values for the effective Hubbard parameter (U_{eff}) and the amount of the non-local exact
110 Hartree-Fock exchange used within the HSE XC functional were tuned according to the value
111 of the ground state electronic band gap and (spin only) magnetic moment of the respective Cu
112 atoms. Excitonic and spin-orbit coupling effects were not taken into account.

113 The formation energy of a defect X in charge state q is defined as [45, 46]:

$$E^f[X^q] = E_{\text{tot}}[X^q] - E_{\text{tot}}[\text{bulk}] - \sum_i n_i \mu_i + q(E_F + \varepsilon^{\text{H}}_{\text{VBM}}) + E_{\text{corr}}. \quad (1)$$

114 $E_{\text{tot}}[X]$ is the total energy derived from a supercell calculation containing the defect X, and
115 $E_{\text{tot}}[\text{bulk}]$ is the total energy for the perfect crystal using an equivalent supercell. The integer n_i
116 indicates the number of atoms of type i (host atoms or impurity atoms) that have been added to
117 ($n_i > 0$) or removed from ($n_i < 0$) the supercell to form the defect, and μ_i are the corresponding
118 chemical potentials of the considered species (related through $\Delta\mu_i = \mu_i - \mu_i^\circ$, where μ_{i}° is the
119 chemical potential of the element i in its standard phase). The chemical potentials represent
120 the energy of the reservoirs with which atoms are being exchanged. E_F represents the electron
121 chemical potential, which ranges from the valence to the conduction band edges, $\varepsilon^{\text{H}}_{\text{VBM}}$ is the
122 eigenvalue of the valence band maximum of the pristine bulk material. Finally, E_{corr} is a
123 correction term that accounts for finite-size effect in the calculations of charged defects as well
124 as aligning of the band edges between the bulk and the defective supercells, performed using the
125 `SXDEFECTALIGN` code by Freysoldt *et al* [47]. The thermodynamic transition levels (ionization
126 levels) of a given defect, $\varepsilon(q_1/q_2)$, correspond to the Fermi-level position at which a given defect
127 changes from one charge state (q_1) to another (q_2):

$$\varepsilon(q_1/q_2) = \frac{E^f[X^{q_1}] - E^f[X^{q_2}]}{q_2 - q_1}. \quad (2)$$

128 The allowed values of $\Delta\mu_i$ are determined from a set of thermodynamic limits. The upper
129 limit is given by $\Delta\mu_i \leq 0$ where element i precipitates to its standard state, e.g., O_2(g) (referred
130 to half of the total energy of an oxygen molecule) and Cu(s). Also, to avoid the formation of
131 secondary solids, the chemical potentials must also be bound by:

$$2\Delta\mu_{\text{Cu}} + \Delta\mu_{\text{O}} \leq \Delta H_{\text{f}}(\text{Cu}_2\text{O}), \quad (3)$$

$$4\Delta\mu_{\text{Cu}} + 3\Delta\mu_{\text{O}} \leq \Delta H_{\text{f}}(\text{Cu}_4\text{O}_3), \quad (4)$$

132 with ΔH_{f} being the standard enthalpy of formation at zero K. The total energies of the phases
133 competing with CuO, i.e., Cu_2O and Cu_4O_3, were calculated using their respective unit cells.
134 Cu_2O was modelled in a simple cubic non-magnetic cell, while for tetragonal Cu_4O_3, a primitive

135 cell containing 14 atoms was used together with the antiferromagnetic spin ordering leading to
136 the observed lowest energy configuration [48–50]. The calculated formation energies of CuO,
137 Cu_2O and Cu_4O_3 read -1.58 eV (1.35 eV), -1.70 eV (-1.46 eV), and -4.85 eV (-4.15 eV) calculated
138 using DFT+U (HSE) and are considerably close to experimental values of 1.59 eV [51], -1.75 eV
139 [51], and -4.88 eV [52], respectively.

140 In the case of CuO passivation, the solubility of the H species were limited by the formation
141 of an additional compound, copper(II) hydroxide:

$$\Delta\mu_{\mathrm{Cu}} + 2\Delta\mu_{\mathrm{O}} + 2\Delta\mu_{\mathrm{H}} = \Delta H_{\mathrm{f}}\big(\mathrm{Cu(OH)_2}\big). \tag{5}$$

142 3 Results and discussion

143 3.1 Modelling magnetic CuO

144 CuO crystallizes in a lower symmetry monoclinic crystal structure (space group $C2/c$, Num-
145 ber 15), compared to Cu_2O. The conventional unit cell consists of eight atoms, four Cu atoms
146 and four O atoms. Each copper atom is coordinated by four oxygen atoms in an approximately
147 square planar configuration, while each oxygen atom is located at the centre of a distorted tetra-
148 hedron [53], with the following lattice parameters: a = 4.6837 Å, b = 3.4226 Å, c = 5.1288 Å [54].
149 Below 230 K, the magnetic ground state of CuO is a peculiar antiferromagnetic arrangement.
150 This ordering is described within an eight-formula magnetic unit cell whose lattice vectors are
151 obtained by expanding the conventional unit cell lattice vectors via the relation $\mathbf{a}' = \mathbf{a} + \mathbf{c}$,
152 $\mathbf{b}' = \mathbf{b}$, and $\mathbf{c}' = -\mathbf{a} + \mathbf{c}$ [6].

153 As previously demonstrated by Rödl *et al* [6], the local magnetic moments that occur both
154 on the Cu and O atoms, as well as the electronic band gap, can be tuned depending on the
155 screened exchange parameter (α) in hybrid (HSE), or as a function of the on-site interaction
156 U in PBE+U calculations. Moreover, a majority of works available in the literature employ
157 experimental lattice parameters within their simulations, which ensures consistency between
158 calculated and experimental crystal structures. However, experimental geometries are (usually)
159 not identical to minimum-energy geometries obtained by structural relaxations within a given
160 functional. This issue is particularly pronounced when hybrid density functionals are employed
161 [55], where calculation time increases dramatically (in the range of a thousand-fold) and system
162 size is limited to a few dozen atoms.

163 In order to examine the underlying effects of strain remnants within the magnetic CuO
164 simulation cell, various pre-relaxed, atomically-relaxed, and fully-relaxed geometries were tested
165 and their validity assessed. Furthermore, two differently ordered spin arrangements of the Cu^{2+}
166 ions in CuO were considered, one along the z axis (AF_Z, the most stable magnetic state) and one
167 along the x axis (AF_X). These were taken following the nomenclature outlined by Rocquefelte
168 *et al* [1] to allow for easier comparison and validation with earlier works.

169 First, the influence of the U_{eff} parameter within DFT+U and the exact exchange α within
170 hybrid DFT on the electronic (Kohn-Sham) band gap were assessed. Results for the two distinct
171 magnetic arrangements are summarized in Figure 2. Note the different values of U_{eff} and α
172 when fitting to the electronic band gap. For a fit to the low temperature band gap value of

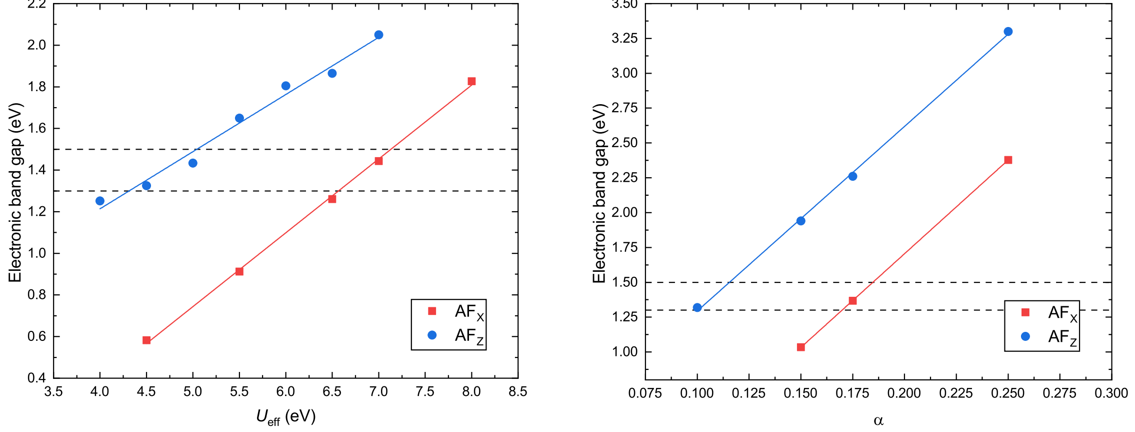

Figure 2: The electronic band gap dependence on the effective U parameter within DFT+U (left) and the exact exchange amount α used for hybrid DFT calculations (right). The red filled squares refer to the AF_X magnetic arrangement, while the blue filled dots represent the AF_Z magnetic configuration. The linear fit is merely an eye-guide for easier data readout. The dashed black lines indicate the range of experimentally available low-temperature values.

173 $1.3 - 1.5\,\text{eV}$ [56], a value of $U_{\text{eff}} = 5\,\text{eV}$ and $U_{\text{eff}} = 7\,\text{eV}$ can be read for the AF_Z and AF_X
174 magnetic ordering, respectively. Similarly, for hybrid DFT calculations, values of $\alpha \approx 0.125$
175 and $\alpha \approx 0.175$ used within HSE are read for AF_Z and AF_X. This explains the variety of U_{eff}
176 and α values in the existing literature that were used for bulk CuO calculations. Together
177 with the choice of an appropriate simulation cell and magnetic arrangement, defining a unique
178 simulation setup becomes a question of the physical properties under examination.

179 Furthermore, so far the simulation have included relaxation effects only up to the atomic
180 position level, i.e., lattice parameters and the cell volume were kept fixed. Starting from the
181 experimental lattice parameters of the CuO magnetic unit cell with two different magnetic
182 arrangements, calculations allowing for lattice cell shape relaxation were performed, in or-
183 der to circumvent the observed internal pressure left within the geometry of the system after
184 only atomic relaxation was performed. The pressure was in certain cases as high as $\pm 2\,\text{GPa}$
185 ($20\,\text{kBar}$), depending on the system under study. Such values are large enough to drive lat-
186 tice instabilities and subsequent structural phase transitions [57]. Thus, care must be taken in
187 order to avoid and minimize internal lattice stress when dealing with CuO. Results of those
188 simulations are illustrated in Figure 3. Based on those results and discussion outlined above,
189 values of $U_{\text{eff}} = 5.5\,\text{eV}$ for DFT+U and $\alpha = 0.125$ for HSE were chosen for this study, as they
190 reproduce the electronic band gap and magnetic moments values accurately, minimizing the
191 internal pressure simultaneously. Surprisingly, allowing for the lattice parameters to change
192 during the relaxation run of AF_X, the calculations proceed in such way that it converges to the
193 AF_Z geometry, indirectly confirming the most stable magnetic configuration.

194 3.2 Intrinsic defects of CuO

195 To explore the native defects in CuO, an antiferromagnetic $2 \times 3 \times 2$ supercell (starting from the
196 magnetic unit cell) was created, which ensures minimal interaction between introduced defects,
197 located at least $10\,\text{Å}$ apart in each crystallographic direction. Furthermore, the differences
198 between DFT+U and HSE values of defect formation energies and impurity band positions

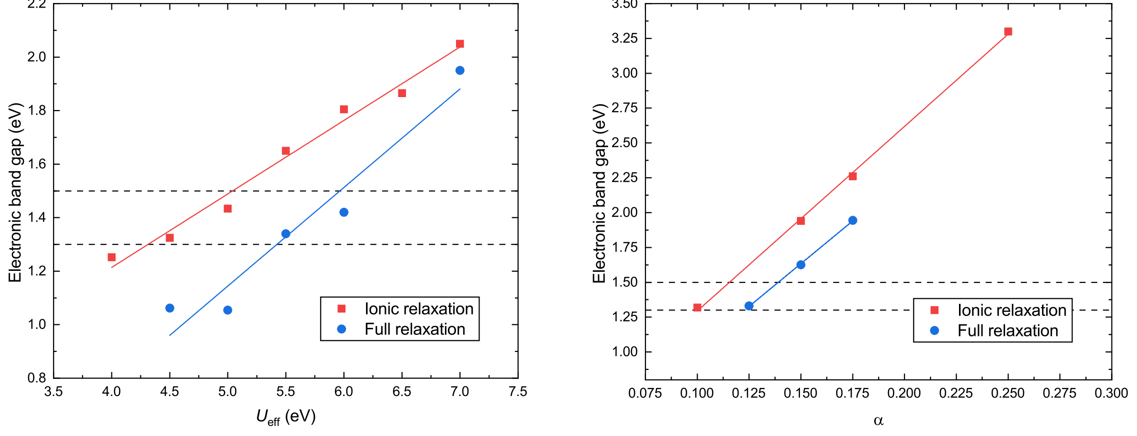

Figure 3: The electronic band gap dependence on the effective U parameter (left) and the exact exchange amount α (right) for the AF_Z configuration. The red filled squares refer to the atomically relaxed geometry, while the blue filled dots represent the fully relaxed geometry (incorporating atomic, cell, and volume relaxation). The linear fit is merely an eye-guide for easier data readout. The dashed black lines indicate the range of experimentally available low-temperature values.

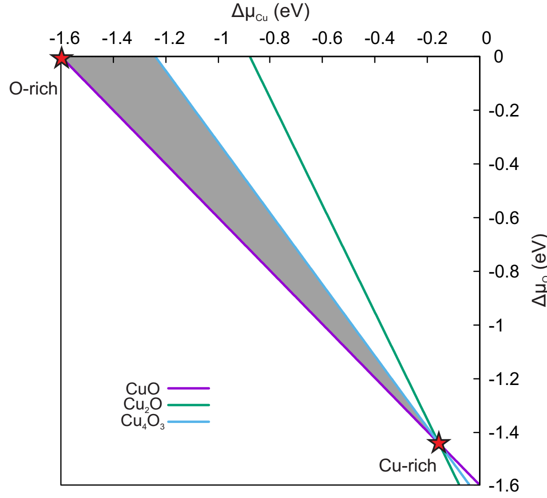

Figure 4: CuO stability limits in the range of allowed chemical potentials, emphasized within the grey-shaded area. The points highlighted with red stars indicate the chemical potential taken for the calculations to be carried out. Values were calculated from experimental formation enthalpies in order to assure transferability of results.

within the electronic structure are examined.

Phase stability Following the formalism outlined in equations (1)–(4), the boundaries for chemical potentials were calculated and shown in Figure 4. To analyse the effect of employed growth conditions on undoped CuO samples, two chemical potential limits were chosen: one with O-rich/Cu-poor and the other with Cu-rich/O-poor conditions. The selected values read:

- O-rich/Cu-poor: $\Delta\mu(\mathrm{Cu}) = -1.594$, $\Delta\mu(\mathrm{O}) = 0.000$.
- Cu-rich/O-poor: $\Delta\mu(\mathrm{Cu}) = -0.157$, $\Delta\mu(\mathrm{O}) = -1.437$.

Simple native defects were introduced into the CuO magnetic supercell, including simple vacancies (labelled V_{Cu} and V_O), anti-sites (Cu_O and O_{Cu}), and interstitials in various positions within the cell (Cu_i and O_i).

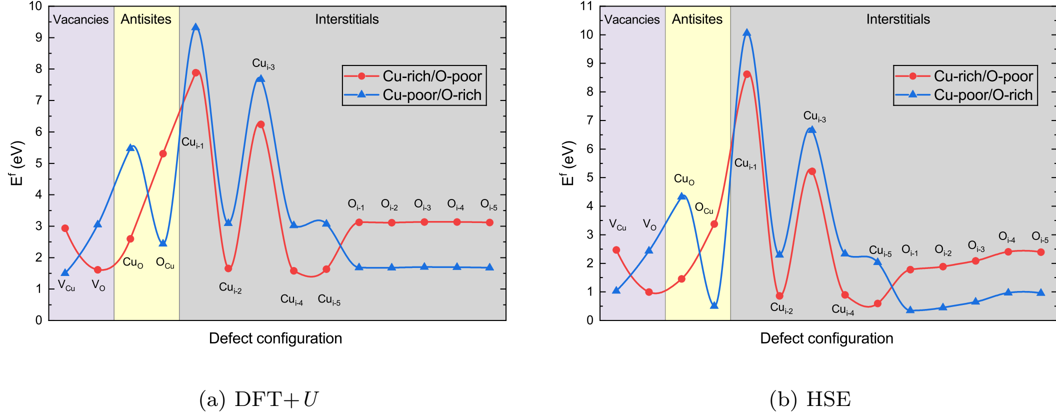

Figure 5: Calculated formation energies of simple native defects in CuO under different chemical potential limits, using two types of approximation for the XC functional. Symbols are the calculated values; the lines are aides to guide the eye.

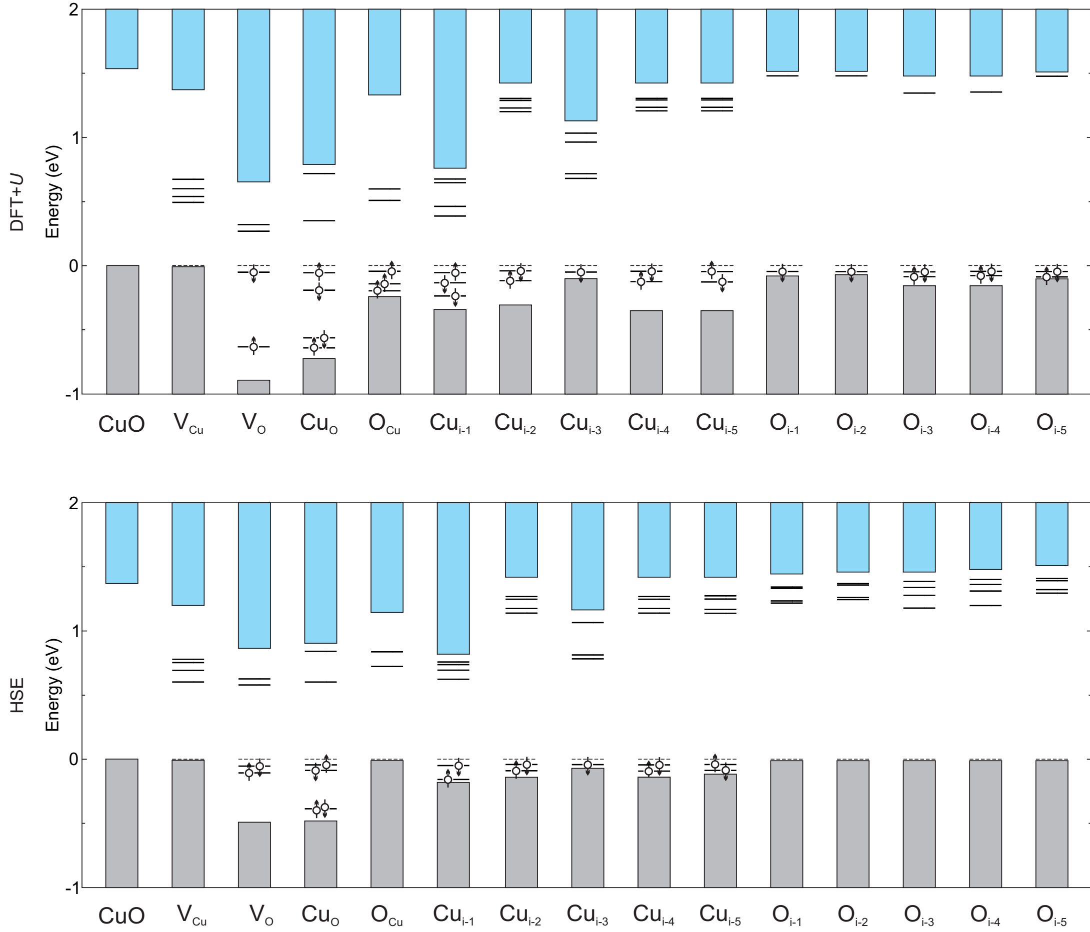

Figure 6: A cumulative schematic representation drawn from electronic densities of state (DOS) data calculated for clean and defective CuO. A comparison between DFT+U and HSE calculated values is illustrated in the top and bottom row. The grey and light-blue rectangular shapes correspond to the valence and conductions band, respectively, while short lines indicate positions of defect levels obtained from DFT+U and HSE calculations. The dashed line indicates the highest occupied band and up/down arrows represent different spin channels.

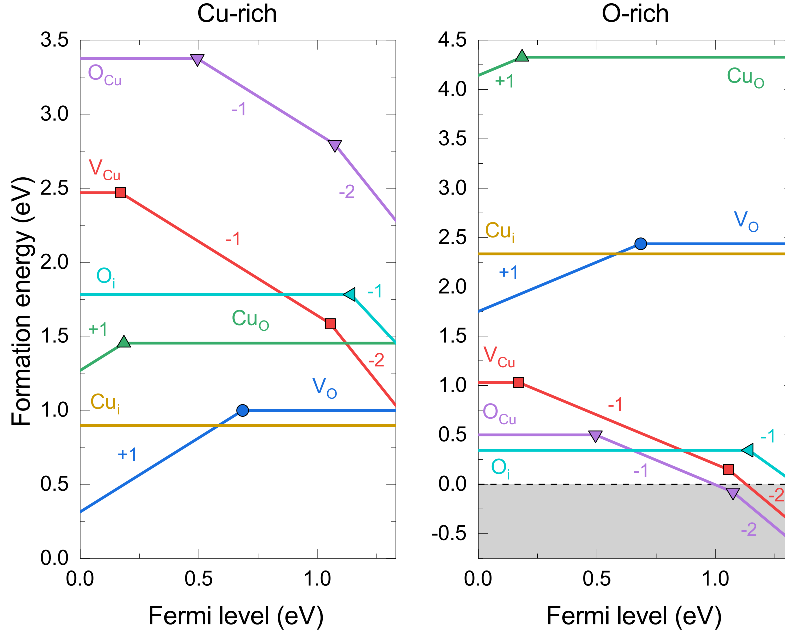

Figure 7: Calculated defect formation energies as a function of the Fermi-level position of native defects occurring in CuO under different chemical potential limits. The slope of the lines denotes the charge state and the solid dots represent the transition levels ε.

209 **Intrinsic defects** Figure 5 displays the neutral formation energies for all the possible intrinsic
210 defects occurring in CuO. It is observed that the formation energy of defects varies depending
211 on growth environments, but features overall similar trends between DFT+U and HSE. Under
212 Cu-rich growth environments, the most favourable neutral defects are V_O and Cu_i, with the
213 hindmost depending on the position within the cell. On the other hand, under O-rich conditions,
214 p-type defects V_{Cu}, O_{Cu}, and O_i (which unlike their Cu counterparts do not depend on the
215 position within the cell) are favoured over all n-type defects. The differences in formation
216 energies between distinct growth conditions are large enough to allow for high performance
217 undoped samples of CuO with particular conductivity types to be created.

218 Figure 6 presents a cumulative schematic diagram drawn from electronic densities of state for
219 the considered defects within CuO, obtained using DFT+U and HSE calculations. Similar to
220 the formation energies, the overall trends are consistent between DFT+U and HSE calculations,
221 with the absolute values varying slightly. It is evident that the majority of defects introduces
222 states within the electronic band gap of CuO that are far from the band edges. Such states
223 are detrimental to the operation of devices relying on the promotion of electrons via photon-
224 absorption as they act as recombination centres rather then contributing to an increase in
225 carriers. In order to explore the full potential of intrinsic defects on the carrier generation and
226 compensation processes in CuO, the formation energies of intrinsic defects in various charged
227 states was studies. A plot of the defect formation energy as a function of the Fermi level position
228 for both considered growth environments is plotted in Figure 7. Since the difference between
229 the two utilized methods, DFT+U and HSE, was shown to be small, further discussions concern
230 only results based on HSE calculations.

231 In a Cu-rich environment, the most prominent intrinsic donors are V_O and Cu_i with forma-

232 tion energies around 1 eV. However, V_O behaves as a deep donor with a $\varepsilon(+1/0)$ transition level
233 at 0.69 eV above the valence band maximum (VBM). Such behaviour of V_O in CuO corresponds
234 well to the extremely low carrier mobility of (0.482 − 1.727) $cm^2\,V^{-1}\,s^{-1}$ measured in *n*-type
235 CuO [19]. Cu_i, despite requiring less energy than V_O, forms exclusively as a neutral defect,
236 with its ionization level located in the VBM, and is thus unlikely to provide effective charge
237 compensation in CuO. The lowest energy acceptor defect under Cu-rich conditions is V_{Cu}, yet
238 it lies too high in energy to compensate for the most prominent donor impurities.

239 Under O-rich conditions, acceptor defects dominate the native impurity landscape. The
240 lowest energy acceptor is the O_i, which together with the O_{Cu} and V_{Cu} are all found to form
241 up to 1 eV. Over the whole range of the electronic band gap those are not compensated by
242 any other defects, rendering the material entirely *p*-type in nature. V_{Cu} acts as a relatively
243 shallow acceptor with the $\varepsilon(0/-1)$ transition at 0.17 eV above the VBM and a subsequent
244 deeper $\varepsilon(-1/-2)$ transition at 0.28 eV below the conduction band minimum (CBM). O_{Cu}
245 demonstrates two deep acceptor levels, $\varepsilon(0/-1)$ at 0.49 eV and $\varepsilon(-1/-2)$ at 1.07 eV above the
246 VBM. The calculated $\varepsilon(0/-1)$ transition level of the O_i is found at 1.14 eV above the VBM, thus
247 limiting the otherwise high conductivity that could be expected due to very low cost involved
248 in the formation of these defects.

249 These results confirm the experimentally observed *n*-type conductivity of CuO, assigned to
250 O vacancies and interstitial Cu atoms [19, 20], as well as *p*-type conductivity assigned to Cu va-
251 cancies [21]. Unlike the case of Cu_2O, depending on the growth conditions, CuO can intrinsically
252 be created as an *n*-type (Cu-rich/O-poor environment) or *p*-type (O-rich/Cu-poor environment)
253 semiconductor. However, explored defects present in CuO show states deep in the electronic
254 band gap, thus acting as recombination and trap states rather then carrier concentration and
255 mobility promoters.

256 **The formation of defect pairs** Since a clear trend in occurrence of distinct defects is
257 observed, V_{Cu} or O_i under O-rich and V_O or Cu_i under Cu-rich conditions, the question whether
258 these defects would appear simultaneously. In order to verify this suggestion, defect pairs were
259 introduced into the simulation cell. Pairs were chosen according to the lowest formation energy
260 of their individual appearance under specific growth conditions. In addition, the possibility of
261 clustering effects was analysed by introducing defects in close proximity to each other and as
262 far away as possible across the simulation cell.

263 The calculated formation energies for neutral pairs of defects in CuO is shown in Figure
264 8. From these results, a clear trend of defect clustering over dispersion is noted, regardless of
265 the nature of the defect or employed computational scheme. Furthermore, particular defect
266 formation in close proximity demonstrates a lowering of the formation energy compared to
267 the sum of individual energies. For example, under Cu-rich conditions, the creation of a Cu
268 interstitial next to an already present O vacancy requires an energy of 2.38 eV (1.49 eV), which
269 is lower compared to the sum of individual defect formation energies $E^f(\mathrm{Cu}_i) + E^f(\mathrm{V}_O) =$
270 $1.58\,(0.99)\,\mathrm{eV} + 1.61\,(0.89)\,\mathrm{eV} = 3.19\,(1.88)\,\mathrm{eV}$, calculated using DFT+$U$ (HSE).

271 First, the case where defects are maximally dispersed through the cell is analysed. The
272 two defects were placed at a minimum distance of 8.32 Å in the case of $O_i(V_{Cu})$ and 8.44 Å for

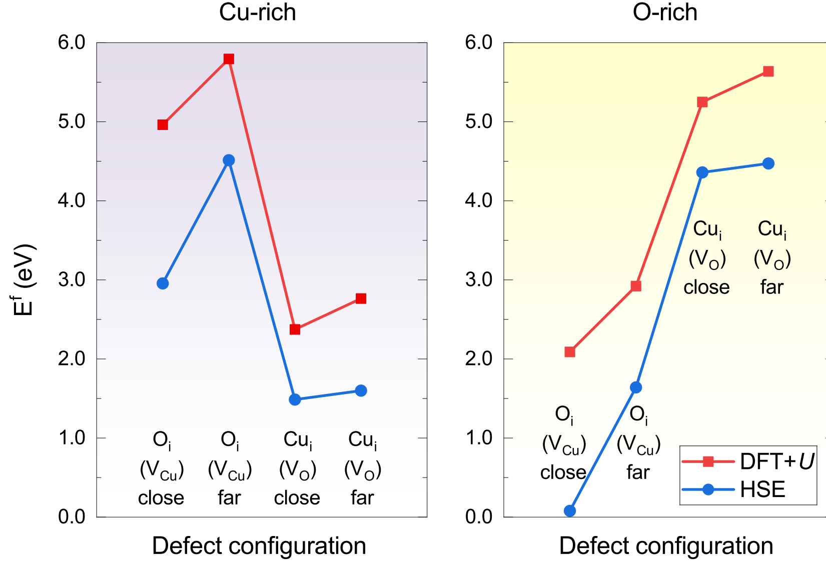

Figure 8: Formation energies for pairs of defects within CuO, under different growth conditions. The used notation specifies a newly induced defect into a cell where the one enclosed in brackets is already present. The pairs were chosen according to the lowest formation energies of individual defects illustrated earlier. A trend to form small clusters can be observed both under Cu-rich and O-rich conditions. Symbols are the calculated values; the lines are aides to guide the eye.

273 $Cu_i(V_O)$, which ensures that the overlap of respective wave functions is minimized as far as
274 possible within the supercell. The notation implies a defect introduced in the host cell where
275 the defect written in brackets was already present. As expected, defects introduced far away
276 across the cell do not interact significantly with each other. They localize around the defect
277 site, creating individual local distortions discussed in earlier paragraphs for single impurities,
278 as observed in the electronic densities of state in Figure 9.

279 Defects occurring in close proximity to each other exhibit different properties compared to
280 their dispersed analogues, due to strong overlap of interacting impurity wave functions. For
281 $O_i(V_{Cu})$, the newly introduced O interstitial atom distorts the structure around the defect site
282 negligibly and forms a weak bond with the nearest lattice O atom (1.37 Å, which is comparable
283 to the separation length of the O_2 molecule of 1.208 Å [58]). $O_i(V_{Cu})$ acts as a deep acceptor,
284 with the $\varepsilon(0/-1)$ and $\varepsilon(-1/-2)$ transition levels found at 0.56 eV and 0.95 eV above the VBM,
285 respectively.

286 In contrast, the addition of Cu_i around an existing V_O defect does not distort the structure
287 significantly. The Cu_i relaxes into the void left behind by the vacancy, easing the bond stress
288 induced by the interstitial on the nearest O and Cu atoms. This allows the structure to relax into
289 a more ordered one, hence lowering the formation energy of the defect complex by almost 0.80 eV
290 (0.40 eV), as indicated before, obtained for DFT+U (HSE). The migration of the interstitial
291 Cu proceeds until a position where the Coulomb repulsion of the surrounding electrons (left
292 behind in the created O vacancy) is minimal. The $Cu_i(V_O)$ complex behaves as a deep donor,
293 analogous to the simple V_O, with the difference that the $\varepsilon(+1/0)$ ionization level is found nearer
294 to the VBM, at 0.34 eV, compared to the individual O vacancy.

295 Following this discussion, a general tendency of defect clustering in CuO is observed. More

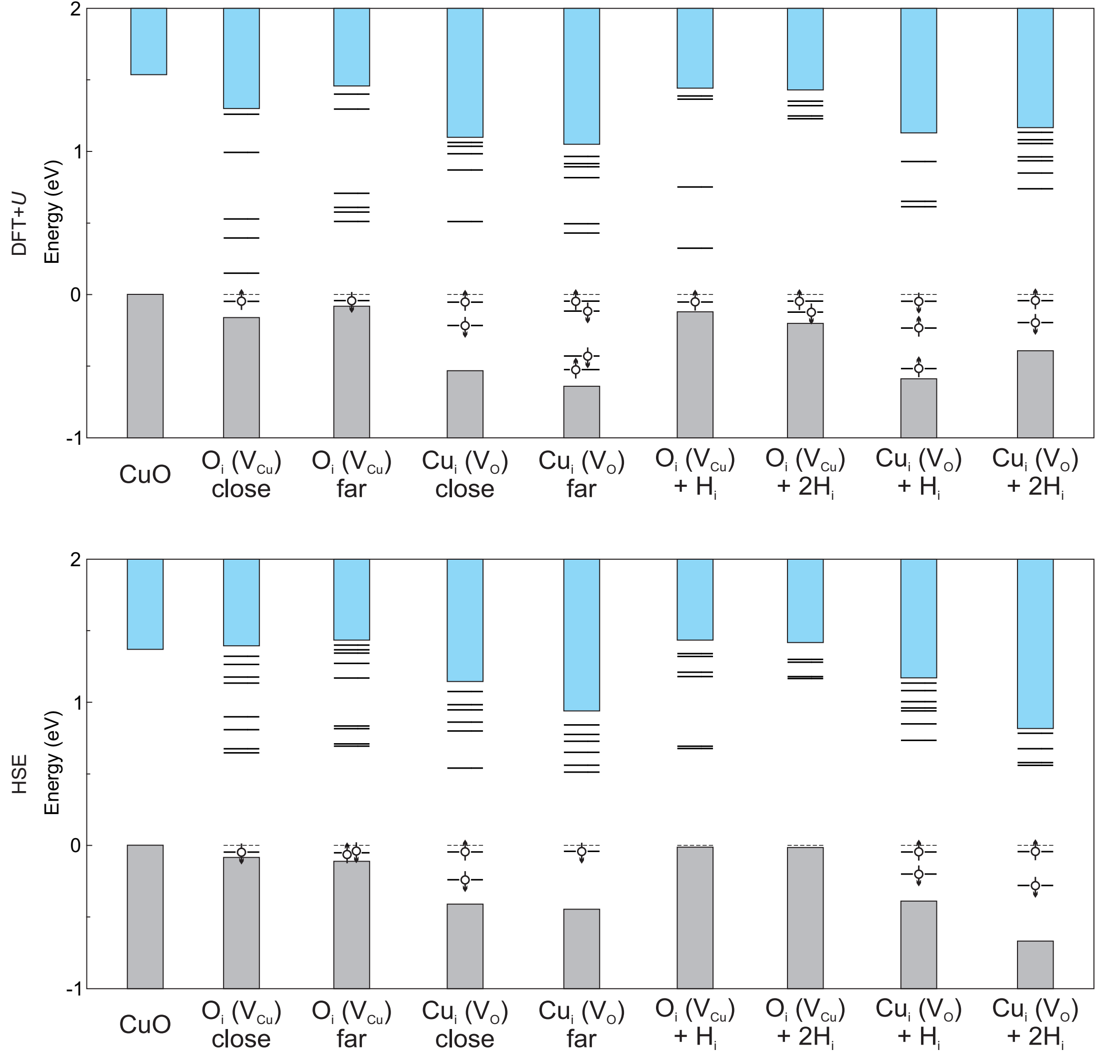

Figure 9: A cumulative schematic representation drawn from electronic densities of state (DOS) data calculated for clean, pairwise defective, and passivated CuO. A comparison between DFT+U and HSE calculated values is illustrated in the top and bottom row. The grey and light-blue rectangular shapes correspond to the valence and conductions band, respectively, while short lines indicate positions of defect levels obtained from DFT+U and HSE calculations. The dashed line indicates the highest occupied band and up/down arrows represent different spin channels.

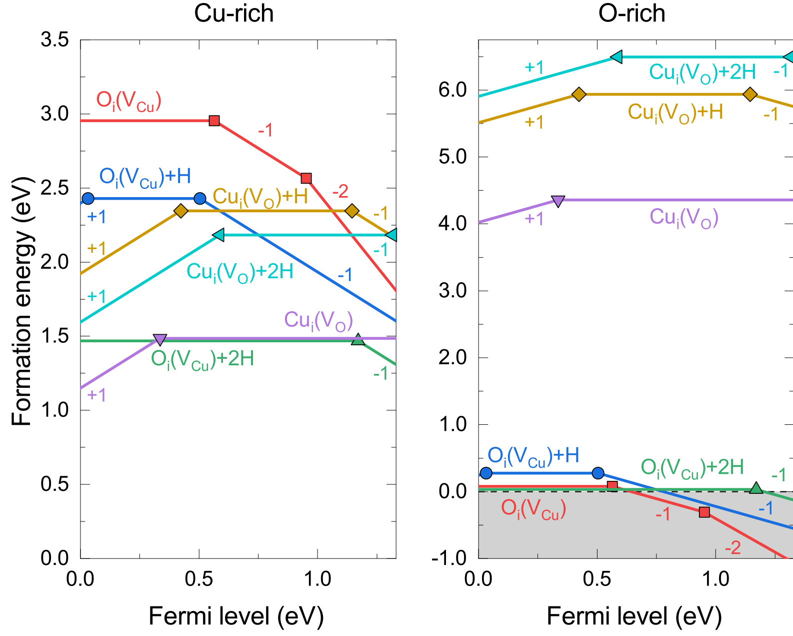

Figure 10: Calculated formation energies as a function of the Fermi-level position of clustered and passivated defects occurring in CuO under different chemical potential limits outlined earlier. The slope of the lines denotes the charge state and the solid dots represent the transition levels ε.

importantly, defects tend to create states located in the middle of the band gap, which is detrimental for any application requiring effective charge capture and separation processes. Deep states favour recombination of created carriers, impairing the overall conductivity, regardless of it being n–type or p–type.

Intentional passivation A further question emerging is whether the mid-gap states created by intrinsic impurities can be removed whilst maintaining the desired conductivity type? One mechanism through which one could influence the character of an impurity is called *passivation*. It explains the often observed compensating nature of defects when donor dopants attract impurities of the opposite kind – acceptors, and vice versa. The resulting complex is often charge neutral and electrically inactive.

In order to test the system for eventual passivation effects, hydrogen was incorporated interstitially into the CuO matrix with the most stable defects present, as identified earlier. Hydrogen was chosen as the simplest possible impurity in order to track the changes that a single electron/hole induce onto the defect complex. Furthermore, the ambiguity when modelling hydrogen is drastically reduced compared to transition metal atoms or complex molecules, which often rely on additional U_{eff} parametrization or exact exchange tuning.

In the initial setup, one H atom is placed into the vacancy site of the $\mathrm{O_i(V_{Cu})}$ defect complex (favouring p–type conductivity). After structural relaxation, the (effectively interstitial) H atom migrates towards the nearest neighbouring O closest to the vacancy site. The H atom binds onto one of the three dangling O bonds left after the $\mathrm{O_i(V_{Cu})}$ defect complex was formed. This removes the strain present in the cell along the c direction and the nearest atoms surrounding the H site relax into their original crystallographic positions in a cell without defects. However,

318 two O dangling bonds along the a–axis remain present, with reduced repulsion effects due to
319 their missing analogues in the perpendicular direction. More importantly, two acceptor states
320 were removed from the electronic structure when compared to the case without interstitial H
321 (Figure 9).

322 Adding a further H atom into the vacancy site of the $\left(O_i(V_{Cu})+H\right)$ complex generates
323 defect behaviour similar to the case of a single interstitial H. The newly added H binds onto its
324 nearest neighbouring O atom left unpaired after the Cu vacancy was created. The surrounding
325 structure remains largely unaffected, with the two interstitial H atoms relaxing away from each
326 other due to active repulsion between identical charges. More importantly, this defect complex
327 configuration leads to removal of the impurity states previously present in the middle of the band
328 gap, leaving an electronic structure similar to that of simple interstitial O atoms, as observed
329 from Figure 9.

330 Figure 10 depicts a plot of the defect formation energy as a function of the Fermi-level
331 position for the H passivated complexes under Cu-rich and O-rich conditions. The singly H
332 passivated $O_i(V_{Cu})$ defect behaves as an amphoteric defect with a shallow $\varepsilon(+1/0)$ transition
333 level 0.03 eV above the VBM and a very deep $\varepsilon(0/-1)$ transition at 0.50 eV above the VBM, ef-
334 fectively killing both p-type and n-type conductivity in the system. However, the $\left(O_i(V_{Cu})+2H\right)$
335 complex is found to have only one level in the band gap, the relatively shallow $\varepsilon(0/-1)$ transi-
336 tion at 0.16 eV below the CBM. This unanticipated finding suggests that a varying amount of
337 incorporated H can lead to substantially different defect behaviour in CuO.

338 These results for CuO indicate consistent behaviour with those of earlier studies on Cu_2O,
339 where a $(H–V_{Cu})$ complex was found to be the most stable defect with a formation energy
340 of only 0.17 eV (results obtained using a HSE functional with 27.5 % of exact exchange) [59].
341 Furthermore, H_i in Cu_2O was found to be an amphoteric impurity under both sets of conditions,
342 suppressing both p–type and n–type conductivity.

343 In the second considered case, interstitial H is placed into the O vacancy site of the $Cu_i(V_O)$
344 complex. This causes the nearest neighbouring Cu atoms to relax away from the interstitial
345 site. The resulting electronic structure remains largely unaltered, as noted from Figure 9.

346 Inserting an additional H into the vacancy site results in a stronger relaxation of surrounding
347 atoms, compared to the single H interstitial. The added H migrates into the layer beneath the
348 O vacancy (along the $-a$ crystallographic axis) binding onto an O atom, causing the nearest
349 neighbouring Cu to relax towards the vacant O site. More importantly, the initial electronic
350 structure of the $Cu_i(V_O)$ complex remains unaffected. The two states remain present in the band
351 gap, as a consequence of the inability of H to counterbalance the larger structural distortion
352 originating from the interstitial Cu atom introduced in the first place. Both the $\left(Cu_i(V_O)+H\right)$
353 and $\left(Cu_i(V_O)+2H\right)$ defect complexes demonstrate amphoteric behaviour, with simultaneous
354 presence of donor and acceptor states in the band gap region. Also, a shifting trend of the
355 $\varepsilon(+1/0)$ and $\varepsilon(0/-1)$ transitions towards higher Fermi-levels can be noted with increasing H
356 concentration.

357 Finally, the difference in passivation effects under different growth environments is dis-
358 cussed. Under O-rich conditions, p-type defects dominate the impurity landscape of H-doped
359 CuO. With an increasing H content, n-type defects are becoming prohibitively expensive to

create, with formation energies reaching more than 6 eV. Thus, interstitial H acts as a *p*-type promoter for CuO created in an O-rich environment. In contrast, under Cu-rich conditions, the formation energy of *n*-type defects increases with H doping, while at the same time the formation energy of *p*-type defects decreases. With increasing H content, the *n*-type defects are not only compensated for, but rather fully replaced by their *p*-type analogues, as observed from Figure 10.

4 Conclusion

A systematic comparative theoretical study of the DFT+U and hybrid–DFT formalism on the electronic and magnetic properties of CuO was undertaken. Various modelling parameters, such as the simulation cell, relaxation type, and magnetic configuration were optimized before the introduction of native point defects, both simple and complex, within the magnetic unit cell of CuO, followed by the evaluation of formation energies, as well as the effect on the overall electronic structure. Following the presented analysis, several significant conclusions can be drawn:

- Both DFT+U and HSE are able to describe the ground state of CuO accurately. However, care is required when tuning either the U parameter in DFT+U or α in HSE accordingly to the type of simulation that is being undertaken.

- Furthermore, both DFT+U and HSE approximation yield similar trends in the formation energies of simple defect that are accessible for CuO.

- Intrinsically, CuO can be created either *p*–type or *n*–type, depending on the synthesis conditions employed. Despite their favourable formation energies, both *p*-type and *n*-type intrinsic defects show states embedded deep in the band gap, clarifying the ineffective photo–response utilization noted experimentally.

- Interstitial H is identified as a *p*-type promoter for CuO created under O-rich conditions, at the same time being detrimental for CuO formed under Cu-rich conditions suppressing all *n*-type intrinsic defects.

One of the main drawbacks while assessing the validity of the results outlined in this chapter is the lack of experimental evidence. Unlike Cu_2O, for which various spectroscopic measurements of intrinsic defects are available, literature for CuO is scarce. Nevertheless, calculations reproduce well the observed conductivity types and the intrinsic defects underpinning them. It is expected that these results will stimulate further experimental attempts to obtain relevant transition levels and doped samples to further optimize the use of CuO as a photo-responsive material.

Acknowledgements

We acknowledge the Cardiff University School of Chemistry for a PhD studentship for AŽ and the Royal Society DfID Africa programme for funding. This work was performed using the

computational facilities of the Advanced Research Computing @ Cardiff (ARCCA) Division, Cardiff University. Via our membership of the UK's HPC Materials Chemistry Consortium, which is funded by EPSRC (EP/L000202, EP/R029431), this work made use of the ARCHER facility, the UK's national high-performance computing service, which is funded by the Office of Science and Technology through EPSRC's High End Computing Programme. Information on the data underpinning the results presented here, including how to access them, can be found in the Cardiff University data catalogue at http://doi.org/10.17035/d.2019.0089582693.

References

[1] X. Rocquefelte, M.-H. Whangbo, A. Villesuzanne, S. Jobic, F. Tran, K. Schwarz, P. Blaha, *J. Phys. Condens. Matter* **2010**, *22*, 045502.

[2] H.-Y. Huang, N. A. Bogdanov, L. Siurakshina, P. Fulde, J. van den Brink, L. Hozoi, *Phys. Rev. B* **2011**, *84*, 235125.

[3] X. Rocquefelte, K. Schwarz, P. Blaha, *Sci. Rep.* **2012**, *2*, 759.

[4] X. Rocquefelte, K. Schwarz, P. Blaha, S. Kumar, J. van den Brink, *Nat. Commun.* **2013**, *4*, 1–7.

[5] A.-M. Pradipto, R. Maurice, N. Guihéry, C. de Graaf, R. Broer, *Phys. Rev. B* **2012**, *85*, 014409.

[6] C. Rödl, F. Sottile, L. Reining, *Phys. Rev. B* **2015**, *91*, 045102.

[7] C. Rödl, K. O. Ruotsalainen, F. Sottile, A.-P. Honkanen, J. M. Ablett, J.-P. Rueff, F. Sirotti, R. Verbeni, A. Al-Zein, L. Reining, S. Huotari, *Phys. Rev. B* **2017**, *95*, 195142.

[8] J. Ghijsen, L. Tjeng, J. van Elp, H. Eskes, J. Westerink, G. Sawatzky, M. Czyzyk, *Phys. Rev. B* **1988**, *38*, 11322–11330.

[9] C. Ekuma, V. Anisimov, J. Moreno, M. Jarrell, *Eur. Phys. J. B* **2014**, *87*, 23.

[10] S. Chatterjee, S. K. Saha, A. J. Pal, *Sol. Energy Mater. Sol. Cells* **2016**, *147*, 17–26.

[11] C. Jayathilaka, V. Kapaklis, W. Siripala, S. Jayanetti, *Appl. Phys. Express* **2015**, *8*, 065503.

[12] L. Yu, A. Zunger, *Phys. Rev. Lett.* **2012**, *108*, 068701.

[13] L. Yu, R. S. Kokenyesi, D. A. Keszler, A. Zunger, *Adv. Energy Mater.* **2013**, *3*, 43–48.

[14] A. Živković, A. Roldan, N. H. de Leeuw, *Phys. Rev. B* **2019**, *99*, 035154.

[15] T. Wong, S. Zhuk, S. Masudy-Panah, G. Dalapati, *Materials (Basel).* **2016**, *9*, 271.

[16] S. Masudy-Panah, K. Radhakrishnan, H. R. Tan, R. Yi, T. I. Wong, G. K. Dalapati, *Sol. Energy Mater. Sol. Cells* **2015**, *140*, 266–274.

[17] S. Masudy-Panah, K. Radhakrishnan, A. Kumar, T. I. Wong, R. Yi, G. K. Dalapati, *J. Appl. Phys.* **2015**, *118*, 225301.

[18] S. H. Lee, M. Shin, S. J. Yun, J. W. Lim, *Prog. Photovoltaics Res. Appl.* **2015**, *23*, 1642–1648.

[19] Y. Du, X. Gao, X. Meng, *Phys. B Condens. Matter* **2019**, *560*, 37–40.

[20] R. Singh, L. Yadav, Shrey, T. Shweta, *Thin Solid Films* **2019**, *685*, 195–203.

[21] Ş. Baturay, A. Tombak, D. Batibay, Y. S. Ocak, *Appl. Surf. Sci.* **2019**, *477*, 91–95.

[22] Z. Wang, L. Zhang, T. U. Schülli, Y. Bai, S. A. Monny, A. Du, L. Wang, *Angew. Chemie Int. Ed.* **2019**, *58*, 17604–17609.

437 [23] M. Nolan, S. D. Elliott, *Phys. Chem. Chem. Phys.* **2006**, *8*, 5350–5358.
438 [24] D. Wu, Q. Zhang, M. Tao, *Phys. Rev. B* **2006**, *73*, 235206.
439 [25] G. Kresse, D. Joubert, *Phys. Rev. B* **1999**, *59*, 1758–1775.
440 [26] P. E. Blöchl, *Phys. Rev. B* **1994**, *50*, 17953–17979.
441 [27] J. P. Perdew, K. Burke, M. Ernzerhof, *Phys. Rev. Lett.* **1996**, *77*, 3865–3868.
442 [28] S. L. Dudarev, G. A. Botton, S. Y. Savrasov, C. J. Humphreys, a. P. Sutton, *Phys. Rev.*
443 *B* **1998**, *57*, 1505–1509.
444 [29] J. Heyd, G. E. Scuseria, M. Ernzerhof, *J. Chem. Phys.* **2003**, *118*, 8207–8215.
445 [30] J. Heyd, G. E. Scuseria, *J. Chem. Phys.* **2004**, *121*, 1187–1192.
446 [31] J. Heyd, G. E. Scuseria, M. Ernzerhof, *J. Chem. Phys.* **2006**, *124*, 219906.
447 [32] S. Grimme, J. Antony, S. Ehrlich, H. Krieg, *J. Chem. Phys.* **2010**, *132*, 154104.
448 [33] H. J. Monkhorst, J. D. Pack, *Phys. Rev. B* **1976**, *13*, 5188–5192.
449 [34] M. I. Aroyo, J. M. Perez-Mato, C. Capillas, E. Kroumova, S. Ivantchev, G. Madariaga,
450 A. Kirov, H. Wondratschek, *Zeitschrift für Krist. - Cryst. Mater.* **2006**, *221*, DOI `10.`
451 `1524/zkri.2006.221.1.15`.
452 [35] M. I. Aroyo, A. Kirov, C. Capillas, J. M. Perez-Mato, H. Wondratschek, *Acta Crystallogr.*
453 *Sect. A Found. Crystallogr.* **2006**, *62*, 115–128.
454 [36] M. I. Aroyo, J. M. Perez-Mato, D. Orobengoa, E. Tasci, G. De La Flor, A. Kirov, *Bulg.*
455 *Chem. Commun.* **2011**, *43*, 183–197.
456 [37] G. Pizzi, D. Volja, B. Kozinsky, M. Fornari, N. Marzari, *Comput. Phys. Commun.* **2014**,
457 *185*, 422–429.
458 [38] G. Pizzi, V. Vitale, R. Arita, S. Bluegel, F. Freimuth, G. Géranton, M. Gibertini, D.
459 Gresch, C. Johnson, T. Koretsune, J. Ibanez, H. Lee, J.-M. Lihm, D. Marchand, A. Mar-
460 razzo, Y. Mokrousov, J. I. Mustafa, Y. Nohara, Y. Nomura, L. Paulatto, S. Ponce, T.
461 Ponweiser, J. Qiao, F. Thöle, S. S. Tsirkin, M. Wierzbowska, N. Marzari, D. Vanderbilt,
462 I. Souza, A. A. Mostofi, J. R. Yates, *J. Phys. Condens. Matter* **2019**, DOI `10.1088/1361-`
463 `648X/ab51ff`.
464 [39] J. Buckeridge, D. Scanlon, A. Walsh, C. Catlow, *Comput. Phys. Commun.* **2014**, *185*,
465 330–338.
466 [40] M. Yu, D. R. Trinkle, *J. Chem. Phys.* **2011**, *134*, 064111.
467 [41] W. Tang, E. Sanville, G. Henkelman, *J. Phys. Condens. Matter* **2009**, *21*, 084204.
468 [42] E. Sanville, S. D. Kenny, R. Smith, G. Henkelman, *J. Comput. Chem.* **2007**, *28*, 899–908.
469 [43] D. Broberg, B. Medasani, N. E. Zimmermann, G. Yu, A. Canning, M. Haranczyk, M.
470 Asta, G. Hautier, *Comput. Phys. Commun.* **2018**, *226*, 165–179.
471 [44] K. Momma, F. Izumi, *J. Appl. Crystallogr.* **2011**, *44*, 1272–1276.
472 [45] C. G. Van De Walle, J. Neugebauer, *J. Appl. Phys.* **2004**, *95*, 3851–3879.
473 [46] S. B. Zhang, J. E. Northrup, *Phys. Rev. Lett.* **1991**, *67*, 2339–2342.
474 [47] C. Freysoldt, J. Neugebauer, C. G. Van de Walle, *Phys. Rev. Lett.* **2009**, *102*, 016402.
475 [48] L. Pinsard-Gaudart, J. Rodríguez-Carvajal, A. Gukasov, P. Monod, *Phys. Rev. B* **2004**,
476 *69*, 104408.
477 [49] D. Djurek, M. Prester, D. Drobac, M. Ivanda, D. Vojta, *J. Magn. Magn. Mater.* **2015**,
478 *373*, 183–187.
479 [50] J. Pierson, E. Duverger, O. Banakh, *J. Solid State Chem.* **2007**, *180*, 968–973.

480 [51] D. R. Lide, *CRC Handbook of Chemistry and Physics, Internet Version 2005*, CRC Press,
481 Boca Raton, Fl, **2005**.

482 [52] K. J. Blobaum, D. Van Heerden, A. J. Wagner, D. H. Fairbrother, T. P. Weihs, *J. Mater.*
483 *Res.* **2003**, *18*, 1535–1542.

484 [53] J. B. Forsyth, S. Hull, *J. Phys. Condens. Matter* **1991**, *3*, 5257–5261.

485 [54] W. Y. Ching, Y. N. Xu, K. W. Wong, *Phys. Rev. B* **1989**, *40*, 7684–7695.

486 [55] J. D. Gouveia, J. Coutinho, *Electron. Struct.* **2019**, *1*, 015008.

487 [56] F. Marabelli, G. B. Parravicini, F. Salghetti-Drioli, *Phys. Rev. B* **1995**, *52*, 1433–1436.

488 [57] C.-M. Hao, Y. Li, Q. Zhu, X.-Y. Chen, Z.-X. Wang, Y.-L. Li, *CrystEngComm* **2018**, *20*,
489 5949–5954.

490 [58] H. Dietrich, *Angew. Chemie* **1961**, *73*, 511–512.

491 [59] D. O. Scanlon, G. W. Watson, *Phys. Rev. Lett.* **2011**, *106*, 186403.